Acta Crystallographica Section B
Structural Science
ISSN 0108-7681

Intra- and intermolecular interactions in small bioactive molecules: cooperative features from experimental and theoretical charge-density analysis

Parthapratim Munshi and Tayur N. Guru Row*

Solid State and Structural Chemistry Unit, Indian Institute of Science, Bangalore 560012, India

Correspondence e-mail: ssctng@sscu.iisc.ernet.in

Received 28 November 2005
Accepted 11 May 2006

The topological features of the charge densities, $\rho(\mathbf{r})$, of three bioactive molecules, 2-thiouracil [2,3-dihydro-2-thioxopyrimidin-4(1*H*)-one], cytosine [4-aminopyrimidin-2(1*H*)-one] monohydrate and salicylic acid (2-hydroxybenzoic acid), have been determined from high-resolution X-ray diffraction data at 90 K. The corresponding results are compared with the periodic theoretical calculations, based on theoretical structure factors, performed using DFT (density-functional theory) at the B3LYP/6-31G** level. The molecules pack in the crystal lattices *via* weak intermolecular interactions as well as strong hydrogen bonds. All the chemical bonds, including the intra- and intermolecular interactions in all three compounds, have been quantitatively described by topological analysis based on Bader's quantum theory of '*Atoms In Molecules*'. The roles of interactions such as C—H···O, C—H···S, C—H···π and $\pi\cdots\pi$ have been investigated quantitatively in the presence of strong hydrogen bonds such as O—H···O, N—H···O and N—H···S, based on the criteria proposed by Koch and Popelier to characterize hydrogen bonds and van der Waals interactions. The features of weak intermolecular interactions, such as S···S in 2-thiouracil, the hydrogen bonds generated from the water molecule in cytosine monohydrate and the formation of the dimer *via* strong hydrogen bonds in salicylic acid, are highlighted on a quantum basis. Three-dimensional electrostatic potentials over the molecular surfaces emphasize the preferable binding sites in the structure and the interaction features of the atoms in the molecules, which are crucial for drug–receptor recognition.

1. Introduction

The rationalization of crystal structures stems from a basic understanding of the nature of molecular interactions, which provide pathways for recognition and packing in the lattice. The link between the molecule and the crystal originates from the intermolecular spaces and the interactions therein. Intermolecular interactions are of enormous importance as they provide for energy minimization in the framework restricted by the crystal symmetry. In this context, hydrogen bonds play a major role since they cover the entire energy range between the covalent bonds and the van der Waals interactions (Desiraju & Steiner, 1999). The analyses of intermolecular interactions, which result in organized flexible and/or rigid frameworks, provide pointers to the design of futuristic materials (Guru Row, 1999). It is of interest to note that researchers in several areas have zoomed in on the features of intermolecular interactions as they provide useful guidelines for structure–activity correlations (Bernstein *et al.*, 1994). The study of weak interactions has evoked enormous interest, as very often these occur in important biological systems such as

carbohydrates (Steiner & Saenger, 1992, 1993), nucleosides (Jeffrey & Saenger, 1991) and proteins (Derewenda *et al.*, 1995; Musah *et al.*, 1997). Many of these systems also possess stronger hydrogen bonds and it is worthwhile evaluating the weak interactions in molecular crystals in the presence of such strong hydrogen bonds. Indeed, such combinations form the basic design elements in crystal engineering (Desiraju, 1991; Braga *et al.*, 1997) as it has been seen in a large number of reports in the literature. A few small bioactive molecules, namely 2-thiouracil, cytosine monohydrate and salicylic acid, were chosen to be the current test cases. The sulfur-containing compound 2-thiouracil is a component in certain nucleic acids and is also a minor component of transfer ribonucleic acid (tRNA). For example, 2-thiouracil has been characterized in $tRNA^{Glu}$ isolated from *Escherichia coli* (Yavin & Folk, 1975). Cytosine is one of the five main nucleobases used to store and transport genetic information within a cell in the nucleic acids DNA and RNA. Salicylic acid is a crystalline organic carboxylic acid, which functions as a plant hormone, especially in fruits (see Wikipedia at http://en.wikipedia.org/wiki/Cytosine and http://en.wikipedia.org/wiki/Salicylic_acid). It is the key additive in many skin-care products for the treatment of acne, keratosis pilaris and warts. The drug–receptor binding sites have proved to be the key component of many small and large biological systems, and the electrostatic requirements at such sites need to be understood.

The measurement of charge densities in molecular crystals using high-resolution single-crystal X-ray diffraction data has now reached a level at which highly reliable theoretical estimates can be compared (Tsirelson & Ozerov, 1996). This has become possible particularly with the advances made in experimental techniques, measuring devices and high-speed computation (Koritsanszky *et al.*, 1998). The importance of the charge-density feature is obvious from Hohenberg–Kohn's theorem (Hohenberg & Kohn, 1964), which states that all ground-state properties are unique functionals of the charge density. The extraction of detailed charge-density distributions of organic, organometallic, inorganic, ionic, metallic and mineral crystalline systems from X-ray diffraction data is now a mature and highly productive field, and one of the most dynamic areas of modern X-ray crystallography (Coppens, 1997; Spackman, 1992, 1997; Koritsanszky & Coppens, 2001).

The Hansen and Coppens formalism (Hansen & Coppens, 1978) is used to represent the multipole model of charge densities. In this model the individual atomic densities are divided into three components: the core, a spherical expansion and contraction term (κ) for the valence shell, and the valence deformation, which is described in terms of density-normalized spherical harmonics ($d_{lm\pm}$), together with the corresponding radial expansion and contraction (κ') of the valence shell as given below

$$\rho_{\rm at}(\mathbf{r}) = P_c\rho_{\rm core}(\mathbf{r}) + P_v\kappa^3\Sigma_{\rm val}(\kappa\mathbf{r}) + \sum_{l=0}^{l_{\max}}\kappa'^3 R_l(\kappa'\mathbf{r})\sum_{m=0}^{l}P_{lm\pm}d_{lm\pm}(\vartheta,\varphi).$$

The core ($\rho_{\rm core}$) and spherical valence ($\rho_{\rm val}$) densities can be calculated from Hartree–Fock (HF) or relativistic HF atomic wavefunctions. The density functions, also referred to as *multipoles*, are the product of *r*-dependent *radial functions* and θ- and φ-dependent *angular functions*. The radial function, $R_l(\kappa' r)$, of the deformation density takes the form of normalized Slater (or Gaussian) functions

$$R_l(\mathbf{r}) = \kappa'^3\frac{\xi^{n_l+3}}{(n_l+2)!}(\kappa'\mathbf{r})^{n(l)}\exp(-\kappa'\xi_l\mathbf{r}).$$

The angular functions are the real spherical harmonic functions, which are the same as those used to describe atomic orbitals. Bader's quantum theory of '*Atoms in Molecules*' (AIM; Bader, 1990, 1998) can be used to interpret the charge density obtained from experimental electron density. It also provides a pathway for comparing the experimental electron density with theoretically derived density in terms of the topological properties of the electron density $\rho(\mathbf{r})$. The line of the highest electron density linking any two atoms is referred to as the 'bond path' (BP) and its length, R_{ij}, is referred to as the 'interaction line'. The bond critical points (BCPs) lie along the bond path with the gradient of the electron density, $\Delta\rho_b(\mathbf{r}) = 0$. The second derivative of the electron density, the *Laplacian* $\nabla^2\rho_b(\mathbf{r})$ ($\sum_{i=1}^{3}$, λ_1, λ_2, λ_3 are the principal curvatures of a bond at the BCP), represents the chemical features of the molecules. If $\nabla^2\rho_b(\mathbf{r}) < 0$, the density is locally concentrated, resulting in shared interactions, while in the case of $\nabla^2\rho_b(\mathbf{r}) > 0$ the electron density is depleted, representing closed-shell interactions. Furthermore, the degree of aromaticity in a particular chemical bond is represented by bond ellipticity, $\varepsilon = (\lambda_1/\lambda_2) - 1$. The electron density, Laplacian, interaction line, the curvatures and the bond ellipticity together represent the topology of the charge-density distribution. With the identification of hydrogen bonds, which provide stabilization energies to varying degrees in a crystalline lattice, the application of topological analysis *via* Bader's quantum theory of AIM (Bader, 1990, 1998) to decipher the nature of such bonds has attracted considerable attention. In order to characterize weak and strong hydrogen bonds and to distinguish these from pure van der Waals interactions in terms of specific properties such as bond order, ionicity and conjugation, Koch and Popelier (hereafter referred to as KP; Koch & Popelier, 1995; Popelier, 2000) have proposed eight criteria. Here the discussions are restricted to the first four criteria only. These criteria establish the formation of hydrogen bonds on a quantum basis. The first condition discusses the presence of a BCP between a donor atom and an acceptor atom linked *via* a bond path. The charge density evaluated at the BCP and its relationship with the overall hydrogen bond energy forms the basis of the second condition. The third condition refers to the positive values of the Laplacian at the BCP, $\nabla^2\rho_b(\mathbf{r})$, and should correlate with the interaction energies. It is possible to relate (Abramov, 1997; Bader, 1990; Espinosa *et al.*, 1998) the charge-density parameters at the BCP to the local electronic kinetic energy density, $G(\mathbf{r}_{\rm CP})$, and the local potential energy density, $V(\mathbf{r}_{\rm CP})$, and hence the total local energy density, $E(\mathbf{r}_{\rm CP})$. The fourth condition deals with the mutual penetra-

tion of the hydrogen and the acceptor atom and compares the non-bonded radii of the donor H atom (r_D^0) and the acceptor atom (r_A^0) with their corresponding bonding radii. The nonbonding radius is taken to be equivalent to the gas-phase van der Waals radius of the participating atoms (Bondi, 1964; Nyburg & Faerman, 1985). The bonding radius (r) is the distance from the nucleus to the BCP. In a typical hydrogen bond, the values of $\Delta = (r_D^0 - r_D) > \Delta = (r_A^0 - r_A)$ and $\Delta r_D + \Delta r_A > 0$ represent positive interpenetration. If either or both of these conditions are violated the interaction is essentially van der Waals in nature.

Here we report the topological features of charge densities from both the experimental and theoretical analysis on three small bioactive molecules: (1) 2-thiouracil [2,3-dihydro-2-thioxopyrimidin-4(1*H*)-one], (2) cytosine [4-aminopyrimidin-2(1*H*)-one] monohydrate and (3) salicylic acid (2-hydroxybenzoic acid). Based on the first four criteria of KP (Koch & Popelier, 1995; Popelier, 2000) and Bader's quantum theory of AIM (Bader, 1990, 1998), the role of weak intermolecular interactions, such as C—H···O, C—H···S, C—H···π and π···π, in the presence of strong hydrogen bonds such as O—H···O, N—H···O and N—H···S, in all the three compounds have been investigated quantitatively for the first time.

2. Experimental

Pure AR-grade quality compounds were procured from Sigma Aldrich. The crystals of 2-thiouracil and cytosine monohydrate were grown as colorless blocks by the slow evaporation of its solution in *N*,*N*-dimethylformamide at room temperature over *ca* 15 d. The needle-like colorless crystals of salicylic acid were grown by slow evaporation from its solution in methanol at low temperature (~ 278 K) in 2 d time. The molecular diagrams of all the three compounds are given below.

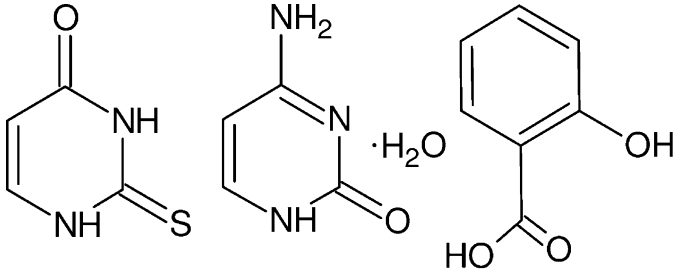

(*a*) 2-Thiouracil (*b*) Cytosine monohydrate (*c*) Salicylic acid

(I)

Good-quality single crystals were selected under an Olympus SZX12 optical microscope equipped with an optical polarizer and an Olympus DP11 digital camera. High-resolution single-crystal X-ray diffraction data were collected on a Bruker AXS SMART APEX CCD diffractometer using Mo $K\alpha$ radiation (50 kV, 40 mA) at 90.0 (2) K (ramp rate 40 K h^{-1}) using an Oxford cryosystem with N_2 flow. Suitable crystals of reasonable sizes (Table 1) were mounted in Lindeman capillaries and allowed to stabilize at the final temperature for 1 h. The data were collected in three steps (Munshi & Guru Row, 2002, 2003; Munshi, 2005) with different scan times (8, 22 and 50 s for 2-thiouracil, 15, 45 and 83 s for cytosine monohydrate, and 20, 40 and 80 s for salicylic acid). Different 2θ settings of the detector (−25, −50 and −75°) and φ settings (0, 90, 180 and 270°) of the goniometer were used and the scanning angle ω was set to 0.3° for each of the 606 frames. The data collection was monitored and reduced with the packages *SMART* (Bruker, 2004) and *SAINTPLUS* (Bruker, 2004), respectively. Sorting, scaling, merging and application of the empirical absorption correction for each set of intensities were performed with *SORTAV* (Blessing, 1987). The structures were solved by direct methods using *SHELXS*97 (Sheldrick, 1997) and refined in the spherical-atom approximation (based on F^2) by using *SHELXL*97 (Sheldrick, 1997) included in the complete package *WinGX* (Farrugia, 1999). The molecular displacement ellipsoid plots were generated using *ORTEP*3 (Johnson, 1965; Farrugia, 1997).

2.1. Multipole refinement

For all three compounds, the multipole refinements were carried out using the module XDLSM incorporated in the software package *XD* (Koritsanszky *et al.*, 2003). Scattering factors were derived from the Clementi & Roetti (1974) wavefunctions for all atoms. The function minimized in the least-squares refinement was for all reflections with $I > 3\sigma(I)$. Initially, only the scale factor was refined with all the reflections. Next, the higher order ($\sin\theta/\lambda \geq 0.8$ Å^{-1}) refinements were performed for the non-H atoms. The positional and isotropic displacement parameters of the H atoms were then refined using the lower-angle data ($\sin\theta/\lambda \leq 0.8$ Å^{-1}). The positions of the H atoms in these refinements, as well as in the subsequent refinements, were fixed to average bond-distance values obtained from reported (Allen, 1986) neutron diffraction studies (*e.g.* N—H 1.03, C_{ar}—H 1.08 and O—H 0.97 Å). For cytosine monohydrate the corresponding values were fixed at the values reported by Weber *et al.* (1980, and references therein) from their neutron diffraction study at 82 K. In the next stage of the refinements, monopole, dipole, quadrupole, octapole and hexadecapole populations, along with a single κ value, were released in a stepwise manner. Finally, a single κ' value was refined for each type of non-H atom, along with the rest of the parameters (including the isotropic displacement parameters of H atoms). For all H atoms the multipole expansion was truncated at the $l_{max} = 1$ (dipole, bond-directed) level. To obtain the best multipole models, for 2-thiouracil only the S atom and for cytosine monohydrate all of the non-H atoms were allowed to refine up to the hexadecapole level, while for salicylic acid the multipole refinement was truncated at octapoles for all non-H atoms. For each chemically different group of the non-H atoms separate κ and κ' values were allowed, while for the H atoms the corresponding values were fixed at 1.2. A similar refinement procedure as described earlier by us (Munshi & Guru Row,

Table 1
Experimental details.

	2-Thiouracil	Cytosine	Salicylic acid
Crystal data			
Chemical formula	$C_4H_4N_2OS$	$C_4H_5N_3O{\cdot}H_2O$	$C_7H_6O_3$
M_r	128.16	129.13	138.12
Cell setting, space group	Triclinic, $P\bar{1}$	Monoclinic, $P2_1/c$	Monoclinic, $P2_1/c$
Temperature (K)	90.0 (2)	90.0 (2)	90.0 (2)
a, b, c (Å)	4.2427 (4), 5.9648 (5), 10.5801 (10)	7.7161 (8), 9.8337 (10), 7.5131 (8)	4.8818 (2), 11.2009 (5), 11.2335 (5)
α, β, γ (°)	105.736 (5), 94.912 (5), 91.927 (4)	90, 100.523 (5), 90	90, 92.621 (2), 90
V (Å^3)	256.32 (4)	560.49 (10)	613.61 (5)
Z	2	4	4
D_x (Mg m^{-3})	1.661	1.530	1.495
Radiation type	Mo $K\alpha$	Mo $K\alpha$	Mo $K\alpha$
No. of reflections for cell parameters	4983	5948	31 354
θ range (°)	3.6–51.6	2.7–50.3	2.6–50.3
μ (mm^{-1})	0.51	0.12	0.12
Crystal form, color	Block, colorless	Block, colorless	Prism, colorless
Crystal size (mm)	0.39 × 0.19 × 0.12	0.32 × 0.22 × 0.03	0.25 × 0.22 × 0.2
Data collection			
Diffractometer	Bruker SMART APEX CCD area detector	Bruker SMART APEX CCD area detector	Bruker SMART APEX CCD area detector
Data collection method	φ and ω scans	φ and ω scans	φ and ω scans
Absorption correction	Multi-scan (based on symmetry-related measurements)	Multi-scan	Multi-scan (based on symmetry-related measurements)
T_{min}	0.831	0.961	0.886
T_{max}	0.943	0.996	0.977
No. of measured, independent and observed reflections	4983, 4983, 4697	5948, 5948, 4792	31 354, 6440, 5439
Criterion for observed reflections	$I > 3\sigma(I)$	$I > 3\sigma(I)$	$I > 3\sigma(I)$
R_{int}	0.031	0.040	0.029
θ_{max} (°)	51.6	50.3	50.3
Range of h, k, l	$0 \Rightarrow h \Rightarrow 9$ $-13 \Rightarrow k \Rightarrow 13$ $-23 \Rightarrow l \Rightarrow 22$	$-16 \Rightarrow h \Rightarrow 16$ $0 \Rightarrow k \Rightarrow 21$ $0 \Rightarrow l \Rightarrow 16$	$-10 \Rightarrow h \Rightarrow 10$ $-23 \Rightarrow k \Rightarrow 24$ $-24 \Rightarrow l \Rightarrow 24$
Refinement			
Refinement on	F^2	F^2	F^2
$R[F^2 > 2\sigma(F^2)]$, $wR(F^2)$, S	0.014, 0.017, 1.93	0.017, 0.015, 1.96	0.020, 0.020, 1.96
N_{obs}/N_{par}	20.51	14.22	19.71
No. of reflections	4697	4792	5439
No. of parameters	229	337	276
H-atom treatment	Not refined	Not refined	Not refined
Weighting scheme	$w2 = 1/[\sigma^2(F_o^2)]$	$w2 = 1/[\sigma^2(F_o^2)]$	$w2 = q/[\sigma^2(F_o^2) + (0.00P)^2 + 0.00P + 0.00 + 0.00\sin(\text{th})]$, where $P = (0.3333F_o^2 + 0.6667F_c^2)$, $q = 1.0$
$(\Delta/\sigma)_{max}$	<0.0001	<0.0001	<0.0001
$\Delta\rho_{max}$, $\Delta\rho_{min}$ (e Å^{-3})	0.32, −0.20	0.27, −0.17	0.27, −0.26

Computer programs used: *SMART*, *SAINT* (Bruker, 2004), *SHELXS*97 (Sheldrick, 1997), *XP* (Koritsanszky *et al.*, 2003).

2002, 2003, 2005*a*,*b*, 2006*a*,*b*; Munshi, 2005) was found to produce a good model of multipole refinement. The scale factor was allowed to refine throughout all the refinements. The modules XDFFT and XDFOUR, implemented in the *XD* (Koritsanszky *et al.*, 2003) package, were used to measure the amount of residual electron density and dynamic deformation density, and hence confirmed the refinement procedure. The module XDPROP of the package *XD* was used for the topological analysis of the electron densities.

2.2. Theoretical calculations

The program *CRYSTAL*03 (Saunders *et al.*, 2003) was used to perform the periodic calculations based on the experimental geometry using the density-functional theory (DFT) method at the B3LYP (Becke, 1993; Lee *et al.*, 1998) level with a 6-31G** basis set (Hariharan & Pople, 1973). This basis set has been used for the studies (Oddershede & Larsen, 2004; Munshi & Guru Row, 2005*a*,*b*, 2006*a*,*b*; Munshi, 2005) related to intermolecular interactions and was found to provide consistent results. The shrinking factors (IS1, IS2 and IS3) along the reciprocal lattice vectors were set at 4 (30 K points in the irreducible Brillouin zone). For all the compounds, the truncation parameters (ITOL) were set as ITOL1 = ITOL2 = ITOL3 = ITOL4 = 6 and ITOL5 = 15, and the level shifter value was set equal to 0.5 Hartree. The temperature factors and atomic positions were held fixed during the multipole refinement of the theoretical structure factors *via XD* (Koritsanszky *et al.*, 2003). The same multipoles as those used in the refinement of the experimental structure factors were allowed to vary, with separate κ' parameters for each non-H atom, including all the theoretical reflections (without any

sigma cut-off). The module XDPROP of the package *XD* was used for the topological analysis of the resulting electron densities.

3. Results and discussion

The unit-cell parameters, experimental details and the multipole refinement parameters, including the residual densities over the asymmetric unit, for all the three compounds are listed in Table 1.[1]

3.1. 2-Thiouracil

The crystal structure of 2-thiouracil at room temperature is known from earlier reports (Tsernoglou, 1967; Tiekink, 1998). Here we re-determine the structure at 90 K. This sulfur-containing compound provides an opportunity to investigate and compare the features associated with the charge densities in the vicinity of the S and O atoms, both being in similar chemical environments. This compound crystallizes in the triclinic system with the centrosymmetric space group $P\bar{1}$ (#2). The molecular *ORTEP* (supporting information, Fig. S1), drawn at 50% probability for the non-H atoms from the data collected at 90 K, shows the atom labeling. Hirshfeld's rigid-bond test (Hirshfeld, 1976) was applied to the covalent bonds during the final refinement. The maximum difference in the mean-square displacement amplitudes (DMSDA) value was found to be 5×10^{-4} Å^2 for the N1—C6 bond, indicating that the atomic thermal vibrations have been properly accounted for. The minimum and maximum residual densities, plotted over the molecular plane (Fig. S2), and the corresponding values over the entire asymmetric unit, given in Table 1, confirm the correctness of the model. It is to be noted that the maximum electron density contours are found to be lying in the vicinity of the S atom, rather than that of the O atom. This observation points out the difficulties encountered in correctly modeling the S atom using multipole analysis (Overgaard & Hibbs, 2004). Earlier Espinosa *et al.* (1997) pointed out that the use of a different set of parameters of the Slater-type sulfur radial function can improve the multipolar model. However, the present study does not take into account such an analysis, but several trials with different refinement strategies improved the model and the present multipole model was selected as the best for the rest of the analyses. The static deformation-density maps obtained from both the experimental and theoretical structure factors are in agreement, as can be seen from Fig. 1. The corresponding dynamic deformation-density map (Fig. S3) indicates the accuracy of the chemical bonding features of the molecule. The lone pairs of electrons on the S and O atoms are prominent in all the maps. The experimental topological parameters of the covalent bonds within the molecule, along with the values obtained from periodic theoretical calculations, for the non-H atoms are given in Table 2. It is noteworthy that the agreement between the experimental and theoretical topological values is in general good, demonstrating that both methodologies provide comparative measures of the topological properties of the charge density. However, a few of them exhibit some discrepancies. Although the location of the BCPs for the C—S and C—C bonds are almost at the middle of the bonds, they lie

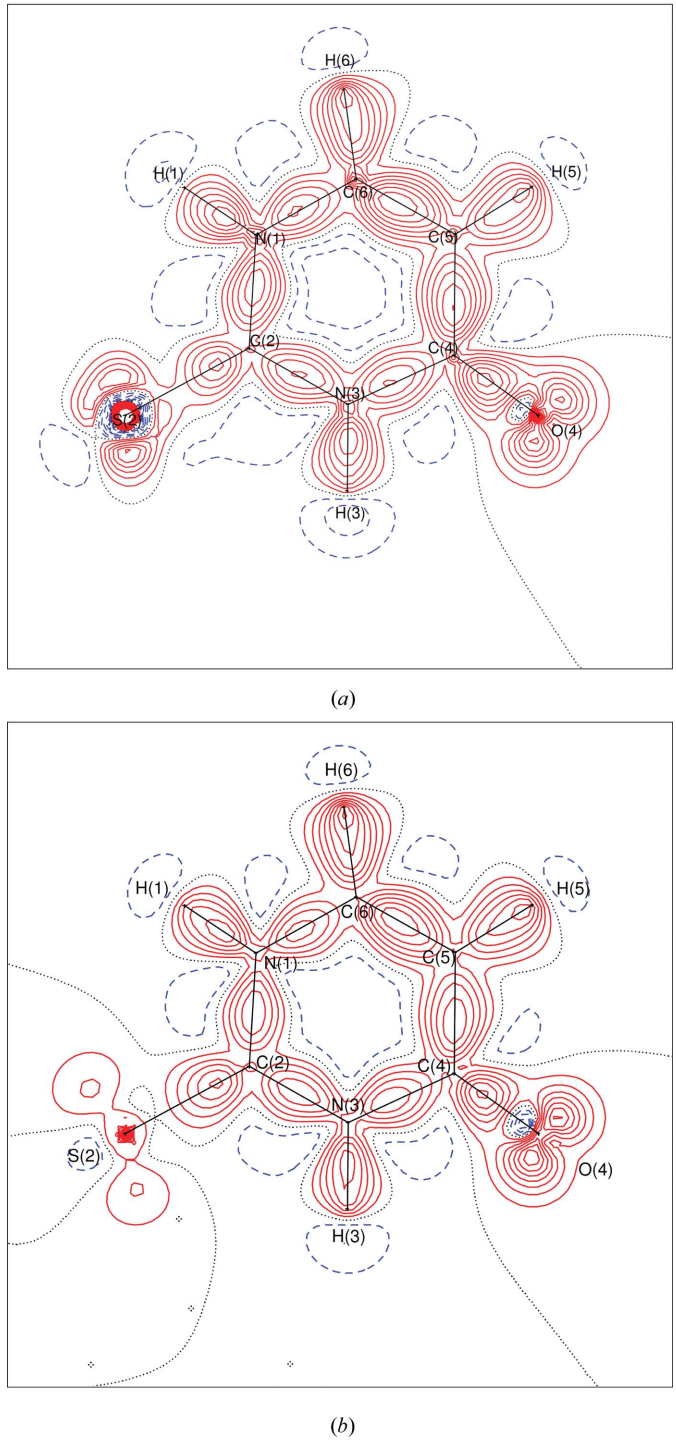

Figure 1
Static deformation-density maps (experimental and theoretical) for 2-thiouracil. For all the static deformation-density maps, the positive (solid red lines) and negative (broken blue lines) contours are with intervals of ± 0.1 e Å^{-3}; the black dotted lines are zero contours.

[1] Supplementary data for this paper are available from the IUCr electronic archives (Reference: LC5044). Services for accessing these data are described at the back of the journal.

Table 2
Bond critical points for covalent bonds of 2-thiouracil (values from the periodic calculation using the B3LYP/6-31G** method are given in italics).

Bonds ($A-B$)	ρ_b	$-\nabla^2\rho_b$	$d1$ ($A-$CP)	$d2$ (CP$-B$)	λ_1	λ_2	λ_3	ε
S2—C2	1.39 (2)	−2.26 (6)	0.796	0.889	−7.23	−5.27	10.2	0.37
	1.46	*−7.63*	*0.780*	*0.899*	*−7.00*	*−6.50*	*5.86*	*0.10*
O4—C4	2.86 (1)	−27.51 (7)	0.807	0.428	−27.00	−23.70	23.20	0.14
	2.74	*−28.72*	*0.790*	*0.451*	*−24.00*	*−21.00*	*16.30*	*0.10*
N1—C2	2.30 (1)	−25.61 (4)	0.813	0.538	−19.00	−15.80	9.19	0.21
	2.24	*−21.07*	0.790	*0.563*	*−18.00*	*−15.00*	*11.70*	*0.20*
N1—C6	2.14 (1)	−19.76 (4)	0.821	0.550	−16.70	−13.60	10.50	0.23
	2.11	*−19.03*	*0.810*	*0.559*	*−16.00*	*−15.00*	*11.20*	*0.10*
N3—C2	2.25 (1)	−23.01 (4)	0.796	0.561	−18.70	−15.20	10.90	0.23
	2.22	*−20.58*	*0.790*	*0.567*	*−17.00*	*−15.00*	*11.90*	*0.10*
N3—C4	2.09 (1)	−18.48 (4)	0.818	0.577	−16.50	−13.50	11.60	0.22
	2.05	*−18.17*	*0.820*	*0.572*	*−16.00*	*−14.00*	*11.50*	*0.10*
C4—C5	2.03 (1)	−17.43 (2)	0.760	0.683	−15.40	−12.20	10.10	0.26
	1.94	*−15.16*	*0.740*	*0.700*	*−14.00*	*−12.00*	*10.60*	*0.20*
C6—C5	2.36 (1)	−23.03 (3)	0.714	0.640	−18.30	−13.60	8.88	0.35
	2.25	*−20.56*	*0.700*	*0.654*	*−17.00*	*−13.00*	*9.48*	*0.30*

Table 3
The parameters characterizing the intermolecular interactions (values from the periodic calculation using the B3LYP/6-31G** method are given in italics).

Interaction	$\Delta r_D - \Delta r_A$	$\Delta r_D + \Delta r_A$	R_{ij}	ρ_b	$\nabla^2\rho_b$	$G(r_{CP})$	$V(r_{CP})$
H3—*X*2···O4	0.259	0.942	1.798	0.16	3.97	86.87	−65.56
$-x, -y+1, -z$	*0.229*	0.944	*1.796*	*0.18*	4.06	92.02	*−73.44*
H1—*X*2···S2	0.242	0.654	2.286	0.08	1.63	34.37	−24.45
$-x+1, -y+2, -z+1$	*0.301*	*0.653*	2.287	*0.13*	*2.02*	*46.51*	*−37.92*
H5—*X*2···O4	0.210	0.446	2.294	0.06	1.30	26.19	−17.06
$-x-1, -y+2, -z$	*0.216*	*0.448*	*2.293*	*0.05*	*1.30*	*25.78*	*−16.29*
H6—*X*1···S2	0.033	0.086	2.854	0.04	0.53	11.28	−8.02
$x-1, +y+1, z$	*0.163*	*0.085*	*2.855*	*0.05*	*0.63*	*13.74*	*−10.27*
H6—*X*1···S2	−0.022	−0.083	3.023	0.04	0.51	10.84	−7.71
$x, +y+1, z$	*0.088*	*−0.067*	*3.007*	*0.05*	*0.57*	*12.67*	*−9.73*
O4—*X*2···C5	−0.238	0.175	3.215	0.04	0.54	11.14	−7.67
$-x, -y+2, -z$	*−0.273*	*0.174*	*3.216*	*0.04*	*0.50*	*10.2*	*−6.86*
C2—*X*1···C5	0.132	0.335	3.365	0.04	0.45	9.34	−6.51
$x+1, +y, z$	*0.079*	*0.279*	*3.421*	*0.04*	*0.42*	*8.88*	*−6.45*
N1—*X*2···N1	0	−0.207	3.407	0.03	0.44	9.02	−5.94
$-x, -y+2, -z+1$	*0*	*−0.207*	*3.407*	*0.03*	*0.46*	*9.34*	*−6.19*
O4—*X*2···O4	0	−0.352	3.431	0.02	0.29	5.69	−3.42
$-x-1, -y+1, -z$	*0*	*−0.351*	*3.431*	*0.02*	*0.27*	*5.13*	*−3.04*
S2—*X*1···N3	0.041	−0.285	3.625	0.03	0.39	8.01	−5.36
$x+1, +y, z$	*−0.064*	*−0.307*	*3.647*	*0.04*	*0.45*	*9.46*	*−6.66*
S2—*X*2···S2	0	−0.156	3.636	0.03	0.36	7.44	−5.16
$-x+1, -y+1, -z+1$	*0*	*−0.156*	*3.636*	*0.05*	*0.44*	*9.90*	*−7.82*

away from the O and N atoms in the case of the C—O and C—N bonds, respectively. The values of $\rho_b(\mathbf{r})$ and $\nabla^2\rho_b(\mathbf{r})$ of the C—S bonds, from both experiment and theory, are rather small in magnitude, which may be interpreted in terms of a very weak, shared interaction between the atoms. The C1—O1 bond appears to be the strongest in terms of the $\rho_b(\mathbf{r})$ and $\nabla^2\rho_b(\mathbf{r})$ values, showing its double-bond character.

The molecules in the crystal lattice are held together *via* strong as well as weak intermolecular interactions. The details of all the parameters characterizing the interactions, purely based on the first four criteria of KP, are given in Table 3. 2-Thiouracil generates intermolecular interactions such as N—H···O, N—H···S, C—H···O (one each) and two C—H···S interactions along with six $\pi\cdots\pi$ interactions involving the non-H atoms present in the structure. The distribution of the charge density and the associated parameters in intermolecular space provide quantitative measures to compare the strength of the interactions. In terms of the total energy density, the N—H···O interaction is found to be the strongest [R_{ij} = 1.8 Å, $E(\mathbf{r}_{CP})$ = 21.31; 18.58 kJ mol^{-1} bohr^{-3}] followed by N—H···S and C—H···O (Table 3). All of these show hydrogen-bond character [$(\Delta r_D + \Delta r_A) > 0$ and $(\Delta r_D - \Delta r_A) > 0$]. Out of the two C—H···S interactions, one shows hydrogen-bond character while the other is van der Waals in nature (Munshi & Guru Row, 2005*c*). However, both show similar values of the parameters related to the electron densities and the energy densities (Table 3). The $\pi\cdots\pi$ interactions are found to be purely of the van der Waals type and they are the weakest in strength among the interactions discussed here. These results are in agreement with several other studies reported in the literature (Espinosa *et al.*, 1998; Espinosa & Molins, 2000; Munshi & Guru Row, 2005*a*,*b*,*c*, 2006*a*). However, the calculation of the *bond degree parameter* (Espinosa *et al.*, 2002), to compare the strength of different H···*X* (*X* = O, N, S) interactions, is another choice. In an effort to bring out the features of the interactions, the BP characteristics and the locations of the (3, −1) BCPs have been highlighted and the distribution of the charge densities in the regions of the intermolecular spaces have been plotted *via* Laplacian maps derived from the experimental analysis. The corresponding maps obtained from theory exhibit similar features (not shown here). Fig. 2 traces the lines of interaction for the C—H···S interaction and it also shows that the N—H···O, N—H···S and C—H···O hydrogen bonds together form dimers and essentially a channel through the structure. The nature of the charge-density distribution in these dimeric regions is shown in the Laplacian maps (Fig. 3). These maps

clearly indicate the differences in the penetrating nature of the H atoms, with respect to the corresponding acceptors, in each case. Fig. 4 shows the nature of the $\pi\cdots\pi$ interactions *via* the BPs and their corresponding BCPs. The corresponding Laplacian maps of the O$\cdots$O and N$\cdots$N interactions show their unique nature (Fig. S4). Fig. 5 shows the Laplacian distribution of the S$\cdots$S interactions. The values of $\rho_b(\mathbf{r})$ and $\nabla^2\rho_b(\mathbf{r})$ for the S$\cdots$S contact, derived from experiment and theory (Table 3), are found to be smaller in magnitude [$\rho_b(\mathbf{r})$ = 0.03 e Å^{-3} and $\nabla^2\rho_b(\mathbf{r})$ = 0.36 e Å^{-5}] than the values [$\rho_b(\mathbf{r})$ = 0.08 e Å^{-3} and $\nabla^2\rho_b(\mathbf{r})$ = 0.53 e Å^{-5}] obtained by Dahaoui *et al.* (1999) from their experimental study on L-cystine. Consequently, the value of R_{ij} = 3.64 Å is found to be larger than in their report (R_{ij} = 3.43 Å). The experimental results agree well with the theoretical calculations in general. Further, based on the important fourth criterion of KP, the values of ($\Delta r_D - \Delta r_A$) $\leq$ 0 from both experiment and theory suggest that this S$\cdots$S contact is of the van der Waals type. The corresponding values of the calculated total energy densities are found to be $\sim$ 2 kJ mol^{-1} bohr^{-3} (Table 3). To the best of our knowledge this is the first report on such interactions analyzed both from experimental and theoretical charge-density studies. It would be interesting to verify these types of interactions from the large number of structures with a different level of theoretical calculations.

3.2. Cytosine monohydrate

The crystal structure of deuterated cytosine monohydrate at 82 K from neutron diffraction has been reported previously by Weber *et al.* (1980, and references therein). Eisenstein (1988) was the first to report the experimental charge-density study on cytosine monohydrate in 1988, followed by Weber & Craven (1990) in 1990. These investigations deal with the exploration of the transferability of the pseudoatomic density in terms of multipole populations rather than directly with the topological analysis. The first study was based on Hirshfeld's (Hirshfeld, 1971, 1977) deformation model, whereas in the second study Stewart's (1976) rigid pseudoatom model was used. The present investigation is based on a multipole analysis *via* the Hansen and Coppens multipole formalism (Hansen & Coppens, 1978), followed by topological analysis of the experimental (X-ray diffraction, 90 K) and theoretical

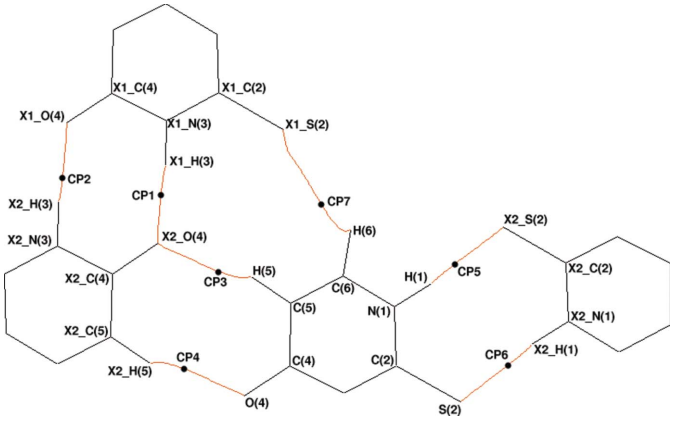

Figure 2
Bond-path character in 2-thiouracil showing the BCP locations along the N—H$\cdots$O, N—H$\cdots$S, C—H$\cdots$O and C—H$\cdots$S interactions.

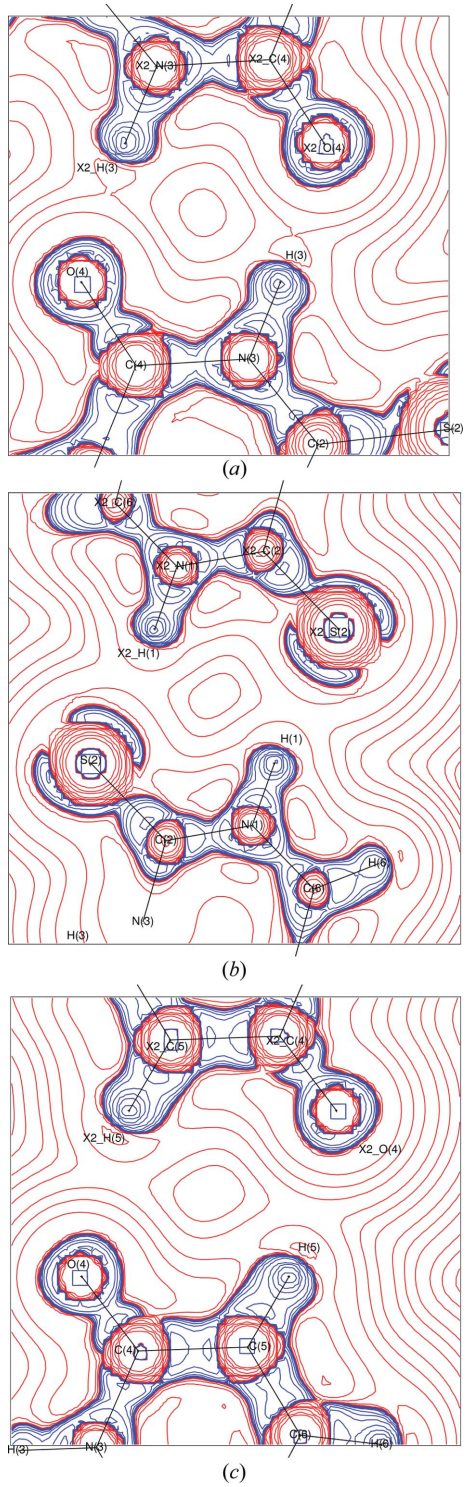

Figure 3
(*a*) Laplacian [$\nabla^2\rho_b(\mathbf{r})$] distribution of the N—H$\cdots$O hydrogen bonds. The contours are drawn at logarithmic intervals of $-\nabla^2\rho_b$ e Å^{-5}. Blue and red lines represent positive and negative contours, respectively. (*b*) Laplacian [$\nabla^2\rho_b(\mathbf{r})$] distribution of the N–H$\cdots$S hydrogen bonds. (*c*) Laplacian [$\nabla^2\rho_b(\mathbf{r})$] distribution of the C—H$\cdots$O hydrogen bonds.

Table 4
Bond critical points for covalent bonds of cytosine monohydrate (values from the periodic calculation using the B3LYP/6-31G** method are given in italics).

Bonds ($A-B$)	ρ_b	$-\nabla^2\rho_b$	$d1$ ($A-$CP)	$d2$ (CP$-B$)	λ_1	λ_2	λ_3	ε
O2—C2	2.95 (2)	−39.77 (10)	0.763	0.498	−29.38	−26.53	16.14	0.11
	2.57	*−19.67*	*0.833*	*0.427*	*−22.23*	*−21.82*	*24.38*	*0.02*
N1—C2	2.36 (1)	−23.45 (6)	0.781	0.592	−20.78	−18.71	16.04	0.11
	2.20	*−22.15*	*0.803*	*0.570*	*−17.24*	*−15.62*	*10.71*	*0.10*
N1—C6	2.41 (2)	−25.54 (7)	0.786	0.573	−21.48	−19.06	14.99	0.13
	2.202	*−20.92*	*0.793*	*0.565*	*−16.76*	*−15.22*	*11.07*	*0.10*
N3—C2	2.49 (1)	−22.23 (6)	0.739	0.615	−21.45	−19.69	18.91	0.09
	2.30	*−20.30*	*0.749*	*0.604*	*−18.37*	*−15.48*	*13.56*	*0.19*
N3—C4	2.48 (2)	−23.31 (7)	0.751	0.594	−21.82	−19.3	17.82	0.13
	2.35	*−20.98*	*0.745*	*0.600*	*−18.19*	*−16.21*	*13.42*	*0.12*
N4—C4	2.51 (1)	−24.56 (7)	0.753	0.581	−22.00	−19.4	16.83	0.13
	2.39	*−26.62*	*0.775*	*0.559*	*−19.86*	*−16.71*	*9.95*	*0.19*
C4—C5	2.09 (1)	−17.46 (4)	0.735	0.697	−16.20	−14.85	13.59	0.09
	2.02	*−17.50*	*0.763*	*0.670*	*−14.11*	*−12.53*	*9.13*	*0.13*
C5—C6	2.39 (1)	−22.27 (5)	0.666	0.690	−19.36	−16.27	13.36	0.19
	2.28	*−21.57*	*0.656*	*0.699*	*−16.39*	*−13.55*	*8.38*	*0.21*

charge densities based on Bader's quantum theory of AIM (Bader, 1990, 1998).

This compound crystallizes with one water molecule in the asymmetric unit, which gives an extra advantage in the study of its intermolecular interactions. The monohydrate crystallizes in the monoclinic system with the centrosymmetric space group $P2_1/c$ (#14). The molecular *ORTEP* plot, drawn at 50% probability for the non-H atoms, from the data collected at 90 K, shows the atom labeling (Fig. S5). The maximum DMSDA value (4×10^{-4} Å^2 for the N1—C6 bond) is within the Hirshfeld limit ($< 10^{-3}$ Å^2) of the rigid-bond test. The almost featureless residual densities over the asymmetric unit (Fig. S6 and Table 1) indicate the quality of the data and the accuracy of the final multipole model. The lone pairs of electrons on the O and N atoms are clearly seen in the dynamic deformation-density map (Fig. S7) and they are also prominent in the experimental and theoretical static deformation-density maps (Fig. 6). The experimental and theoretical topological parameters of the covalent bonds associated with the non-H atoms agree well in general (Table 4). Once again, the location of the BCPs for the C—O and C—N bonds are away from the O and N atoms, respectively, but they are almost at the middle for the C—C bonds. Among these chemical bonds, the C2–O2 bond appears to be the strongest in terms of the $\rho_b(\mathbf{r})$ and R_{ij} values and its double-bond character is obvious from the value of the bond ellipticity, ε.

In this compound the packing of the molecules in the crystal lattice is governed by both the strong and the weak intermolecular interactions. The parameters characterizing these interactions are listed in Table 5. Agreement between the experimental and theoretical values is in general good. The presence of a water molecule plays a major role in arranging the cytosine molecules in the crystal lattice and thereby the molecular packing. The structure contains seven varieties of intermolecular interactions, such as O—H···O, N—H···O, N—H···N and C—H···O, along with four $\pi\cdots\pi$ interactions involving the non-H atoms. Among these, the O atom associated with the water molecule generates four hydrogen-

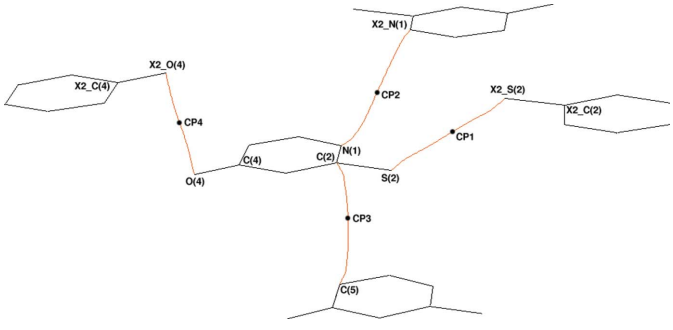

Figure 4
Bond path character in 2-thiouracil showing the BCP locations along the O···O, N···N, S···S and C···C interactions.

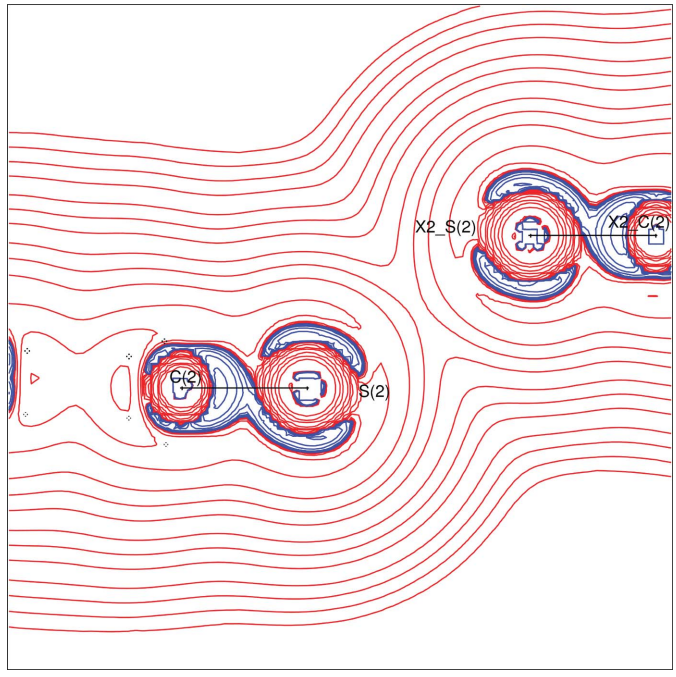

Figure 5
Laplacian $[\nabla^2\rho_b(\mathbf{r})]$ distribution of the S···S intermolecular interaction.

bonding interactions with H atoms, and one interaction with one of the C atoms in the cytosine molecule. Both the H atoms of the water molecule take part in the interactions, with one forming an intramolecular interaction and the other involved in an intermolecular interaction. It is interesting to note that out of the 11 interactions in the structure, the water molecule generates seven. In terms of the characterizing parameters (in particular, the energy density), the O—H···O interaction is found to be the strongest followed by the N—H···N, the two N—H···O and the three C—H···O interactions; almost all have hydrogen-bond character. Out of the three C—H···O interactions, one is of the van der Waals type, while the other two are hydrogen bonds (Table 5). Once again, the $\pi\cdots\pi$ interactions are found to be purely van der Waals in nature and they are weakest of all. The BP characteristics, along with the location of the (3, −1) BCPs and the distribution of the charge density in the region of the intermolecular spaces, plotted *via* Laplacian maps (experimental), clearly highlight these features. Fig. 7 traces the BPs of the O—H···O, N—H···N and N—H···O hydrogen bonds, along with the intramolecular interaction (Table 5) of the water molecule. The interactions generated from the N—H group form the dimer. The nature of the charge-density distributions in this dimeric region is highlighted in the Laplacian map (Fig. S8), which emphasizes the strong hydrogen-bond character of such interactions. The charge-density distribution and the corresponding interactions associated with the water molecule are shown *via* the Laplacian map in Fig. 8. This map illustrates the differences between the distribution of charges in the regions of the intra- and intermolecular interactions. All four intermolecular interactions associated with the O atom in the water molecule, drawn in terms of the BCPs and the BPs, are shown in Fig. 9. The corresponding Laplacian map, in the region where the O atom bifurcates *via* N—H···O and C—H···O hydrogen bonds, is given in Fig. S9. To highlight the nature of the $\pi\cdots\pi$ interactions, the BPs and the location of the corresponding BCPs are shown in Fig. 10. The corresponding Laplacian maps, highlighting the O···C and N···N interactions, are given in Fig. S10. Each map shows the differences in the nature of the interactions and hence the variation in the charge-density distributions.

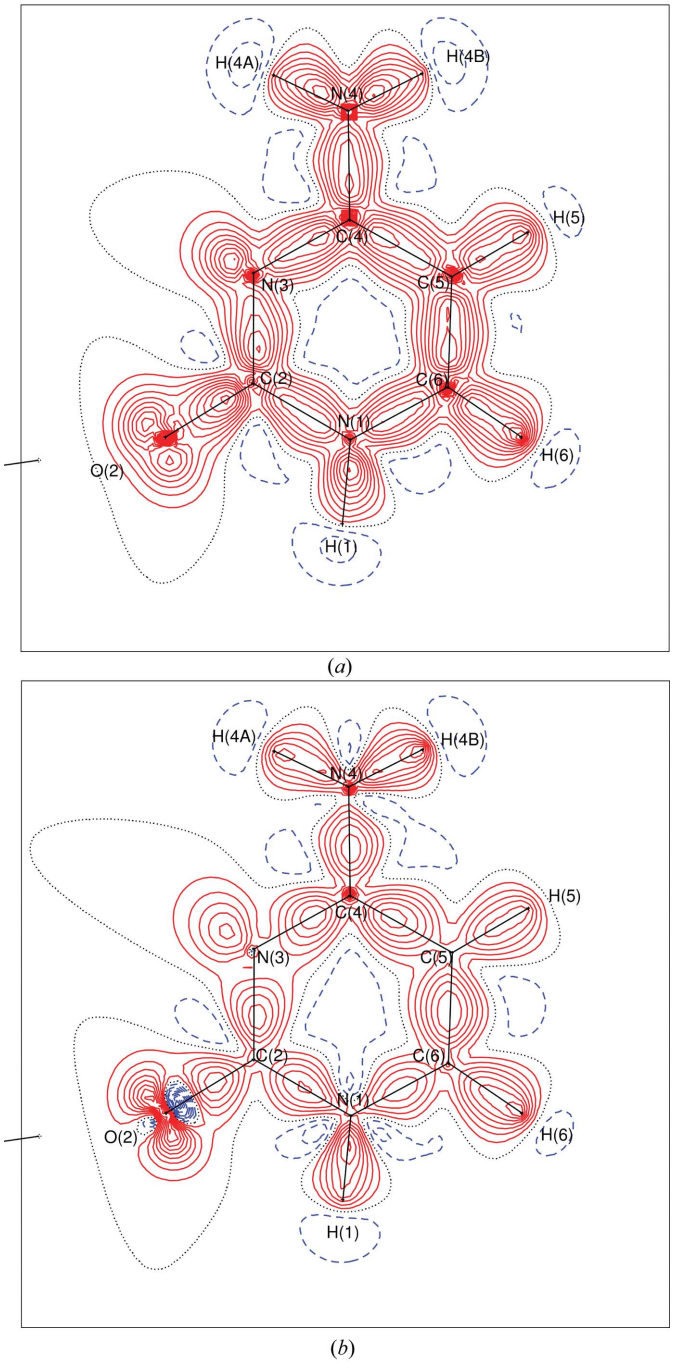

Figure 6
Static deformation-density maps (experimental and theoretical) for cytosine monohydrate.

3.3. Salicylic acid

The previous reports on the crystal and molecular structure (Cochran, 1953) and the refinement of the structure (Sundaralingam & Jensen, 1965) of salicylic acid at room temperature were from data measured by Weissenberg's photographic technique. The present study is based on the X-ray diffraction data collected at 90 K. This compound crys-

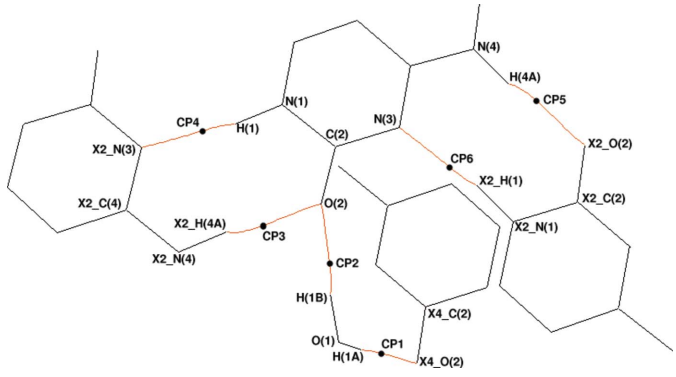

Figure 7
Bond-path character in cytosine monohydrate showing the BCP locations along the O—H···O, N—H···N and N—H···O hydrogen bonds.

Table 5
The parameters characterizing the intra- and intermolecular interactions in cytosine monohydrate (values from the periodic calculation using the B3LYP/6-31G** method are given in italics).

Interaction	$\Delta r_D - \Delta r_A$	$\Delta r_D + \Delta r_A$	R_{ij}	ρ_b	$\nabla^2\rho_b$	$G(r_{CP})$	$V(r_{CP})$
H1*B*—O2	0.271	0.907	1.833	0.12	3.99	81.20	−53.73
x, *y*, *z* (intra)	*0.211*	*0.924*	*1.816*	*0.17*	*3.85*	*85.85*	*−66.93*
H1*A*—*X*4···O2	0.256	0.87	1.870	0.12	3.37	70.84	−49.89
$x, -y+\frac{1}{2}, z-\frac{1}{2}$	*0.196*	*0.876*	*1.864*	*0.18*	*3.35*	*79.33*	*−67.35*
H1—*X*2···N3	0.250	0.884	1.916	0.15	2.94	67.28	−54.4
$-x, y-\frac{1}{2}, -z+\frac{3}{2}$	*0.266*	*0.885*	*1.915*	*0.19*	*3.27*	*78.11*	*−67.24*
H4*B*—*X*4···O1	0.273	0.791	1.949	0.11	2.90	60.85	−42.82
$x-1, -y+\frac{1}{2}, z+\frac{1}{2}$	*0.217*	*0.794*	*1.946*	*0.12*	*2.98*	*62.81*	*−44.54*
H4*A*—*X*2···O2	0.298	0.782	1.958	0.08	2.98	58.79	−36.37
$-x, y+\frac{1}{2}, -z+\frac{3}{2}$	*0.235*	*0.792*	*1.948*	*0.11*	*2.98*	*61.92*	*−42.81*
H5—*X*4···O1	0.107	0.332	2.408	0.07	1.09	23.06	−16.46
$x-1, -y+\frac{1}{2}, z+\frac{1}{2}$	*0.097*	*0.369*	*2.371*	*0.07*	*1.10*	*23.67*	*−17.42*
H6—*X*2···O1	0.205	0.328	2.412	0.05	1.08	21.7	−14.03
$-x, y-\frac{1}{2}, -z+\frac{3}{2}$	*0.185*	*0.352*	*2.388*	*0.06*	*1.08*	*22.64*	*−15.76*
H6—*X*3···O1	−0.041	−0.002	2.742	0.06	0.77	16.49	−11.98
$-x, -y, -z+1$	*−0.065*	*0.022*	*2.718*	*0.06*	*0.78*	*17.01*	*−12.7*
N1—*X*3···N1	0.000	−0.109	3.309	0.04	0.51	10.78	−7.58
$-x, -y, -z+2$	*0.000*	*−0.109*	*3.309*	*0.04*	*0.54*	*11.23*	*−7.72*
N3—*X*4···C4	−0.251	0.064	3.386	0.04	0.40	8.66	−6.35
$x, -y+\frac{1}{2}, z-\frac{1}{2}$	*−0.276*	*0.089*	*3.361*	*0.04*	*0.40*	*8.49*	*−6.17*
O1—*X*1···C5	−0.169	−0.255	3.645	0.02	0.21	4.19	−2.57
$x+1, y, z$	*−0.124*	*−0.262*	*3.652*	*0.02*	*0.21*	*4.18*	*−2.62*
N4—*X*4···C5	−0.243	−0.264	3.714	0.02	0.25	4.91	−3.09
$x, -y+\frac{1}{2}, z-\frac{1}{2}$	*−0.219*	*−0.277*	*3.727*	*0.02*	*0.27*	*5.16*	*−3.11*

tallizes in the monoclinic system with the centrosymmetric space group $P2_1/c$ (#14). Fig. S11 gives the molecular *ORTEP* plot, drawn at 50% probability for the non-H atoms from the data collected at 90 K, and showing the atom labeling. The maximum DMSDA value, 4×10^{-4} Å^2, is found at the C1—C6 bond. The almost featureless minimum and maximum residual densities over the asymmetric unit (Fig. S12), whose values are listed in Table 1, indicate the accuracy of the diffraction data and hence the quality of the final multipole model. The lone pairs of electrons of the O atoms are very prominent in the dynamic deformation-density map (Fig. S13) and also in the experimental and theoretical static deformation-density maps (Fig. 11). These maps show the very similar and accurate features in the covalent bonding regions. The experimental topological parameters (Table 6) of the covalent bonds associated with the non-H atoms are mostly in good agreement with those obtained from theory. The usual trend was observed at the location of the BCPs for the bonds associated with the O atoms in the structure. The BCPs lie away from the O atoms, but almost at the middle of all the C—C bonds. This indicates that the O atoms are larger in size and more polar in nature than the C atoms. As expected, the C7—O2 bond appears to be the strongest in terms of the $\rho_b(\mathbf{r})$ and R_{ij} values obtained from both experiment and theory. Some discrepancies between experiment and theory are also observed for this case.

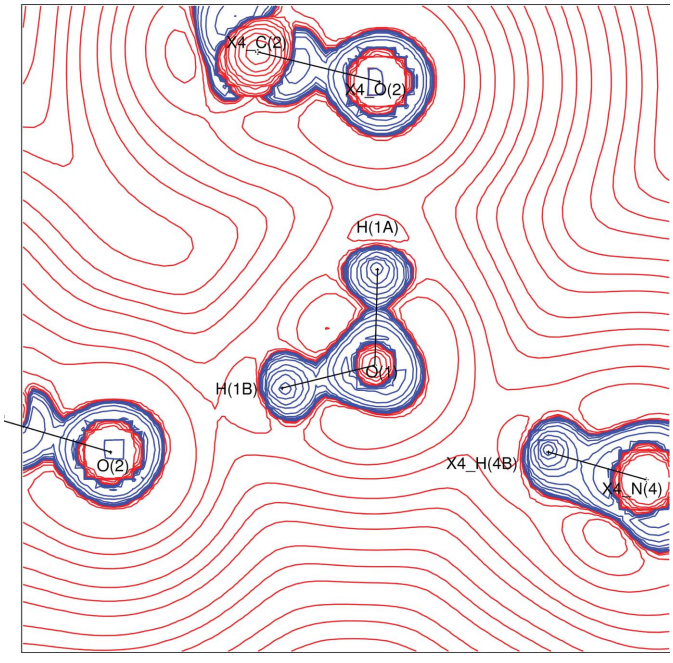

Figure 8
Laplacian $[\nabla^2\rho_b(\mathbf{r})]$ distribution of the O—H···O and N—H···O hydrogen bonds.

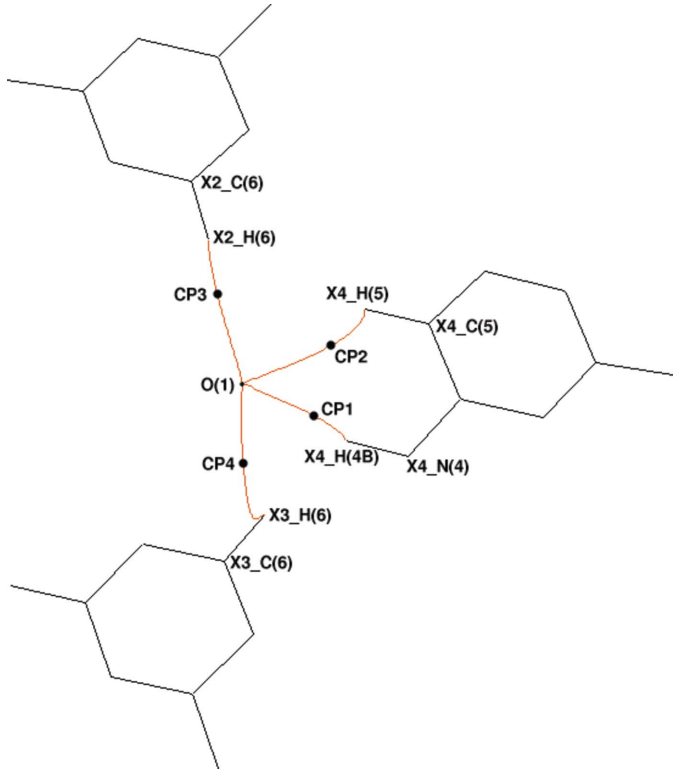

Figure 9
Bond-path character showing the BCP locations along the N—H···O and C—H···O hydrogen bonds.

Table 6
Bond critical points for covalent bonds of salicylic acid (values from the periodic calculation using the B3LYP/6-31G** method are given in italics).

Bonds ($A-B$)	ρ_b	$-\nabla^2\rho_b$	$d1$ ($A-$CP)	$d2$ (CP$-B$)	λ_1	λ_2	λ_3	ε
O1—C7	2.56 (1)	−32.43 (7)	0.823	0.489	−22.94	−20.52	11.03	0.12
	2.21	*−21.49*	*0.833*	*0.478*	*−17.22*	*−15.94*	*11.68*	*0.08*
O3—C2	2.13 (1)	−16.50 (4)	0.802	0.550	−16.89	−16.07	16.46	0.05
	2.02	*−16.54*	*0.821*	*0.531*	*−15.44*	*−13.92*	*12.82*	*0.11*
O2—C7	2.80 (2)	−31.03 (9)	0.802	0.443	−24.84	−23.47	17.29	0.06
	2.73	*−30.38*	*0.801*	*0.444*	*−23.81*	*−22.23*	*15.66*	*0.07*
C1—C6	2.06 (1)	−16.41 (3)	0.714	0.691	−15.27	−12.99	11.85	0.18
	2.02	*−15.24*	*0.697*	*0.708*	*−14.21*	*−11.69*	*10.65*	*0.21*
C1—C2	2.20 (1)	−19.75 (3)	0.688	0.723	−17.57	−13.83	11.65	0.27
	2.09	*−18.23*	*0.677*	*0.734*	*−15.19*	*−12.95*	*9.91*	*0.17*
C1—C7	1.94 (1)	−16.12 (3)	0.703	0.762	−15.07	−12.22	11.17	0.23
	1.87	*−14.51*	*0.687*	*0.779*	*−13.26*	*−11.28*	*10.03*	*0.18*
C3—C2	2.17 (1)	−19.24 (3)	0.669	0.731	−17.24	−13.57	11.56	0.27
	2.12	*−19.18*	*0.669*	*0.731*	*−15.75*	*−13.12*	*9.69*	*0.2*
C3—C4	2.12 (1)	−17.73 (3)	0.692	0.697	−15.75	−13.65	11.68	0.15
	2.09	*−17.42*	*0.683*	*0.706*	*−15.07*	*−12.52*	*10.17*	*0.2*
C6—C5	2.20 (1)	−18.98 (3)	0.696	0.689	−17.05	−13.84	11.92	0.23
	2.18	*−19.40*	*0.712*	*0.673*	*−15.85*	*−13.52*	*9.96*	*0.17*
C5—C4	2.21 (1)	−18.61 (3)	0.706	0.696	−16.83	−13.9	12.12	0.21
	2.07	*−17.56*	*0.708*	*0.695*	*−14.93*	*−12.85*	10.23	*0.16*

The molecules in the crystal lattice are essentially held together *via* weak intermolecular interactions. The details of all the parameters characterizing the interactions are given in Table 7. It has been observed that the experimental and theoretical values agree well in general. The interactions consist of an O—H···O interaction and two C—H···O interactions, along with several $\pi\cdots\pi$ interactions such as O···O, O···C and C···C. The values of the electron-density related parameters listed in Table 7 depict the nature, strength and directionality of these intermolecular interactions. In particular, the hydrogen-bonded regions can be differentiated from the pure van der Waals region. Among these, the O—H···O interaction is found to be the strongest, followed by the two C—H···O interactions. However, all of these interactions show hydrogen-bond character. The energy densities associated with the O—H···O hydrogen bond are much higher than those of the others. In fact, among the interactions discussed in this article, this is the strongest in terms of the characterizing parameters. There are two O···O, five O···C and only one C···C interaction, and all of them are purely van der Waals in nature. The corresponding energy densities vary in the range 2–4 kJ mol^{-1} bohr^{-3}. The features of the interactions are highlighted by the BP characteristics, along with the location of the (3, −1) BCPs and the distribution of the charge density in the regions of the intermolecular spaces plotted *via* Laplacian maps (experimental). All of the hydrogen bonds are shown in Fig. 12, which traces the lines of interactions and the corresponding BCPs for O—H···O and C—H···O hydrogen bonds, along with an intramolecular interaction (Table 7) centered at O2. Out of the three O atoms, the O2 atom forms a dimer *via* the O—H···O hydrogen bonds, while the O1 and O3 atoms each generate one C—H···O hydrogen bond. Fig. 13 shows the corresponding Laplacian distribution of the charge density in the region of the dimer, formed *via* the O—H···O hydrogen bonds. The lines of the contours merge, clearly emphasizing the features associated with strong hydrogen bonds. The Laplacian distribution in one of the C—H···O hydrogen bonds is shown in Fig. S14. Its features are clearly different from the Laplacian of the O—H···O hydrogen bond. Fig. 14 traces the BPs of all the $\pi\cdots\pi$ interactions along with the corresponding (3, −1) BCPs. It is interesting to note that the C7—O2 bond is involved in a $\pi\cdots\pi$ interaction. The bonds interact in a zigzag fashion, *via* two C···O and one O···O interactions, essentially forming a dimer. The corresponding charge-density distribution in this region is shown in the Laplacian map (Fig. S15), which clearly highlights the nature of the $\pi\cdots\pi$ interactions. It is to be noted that both O1 and O2 are trifurcated *via* two C···O and one O···O interactions in each case (Fig. 14).

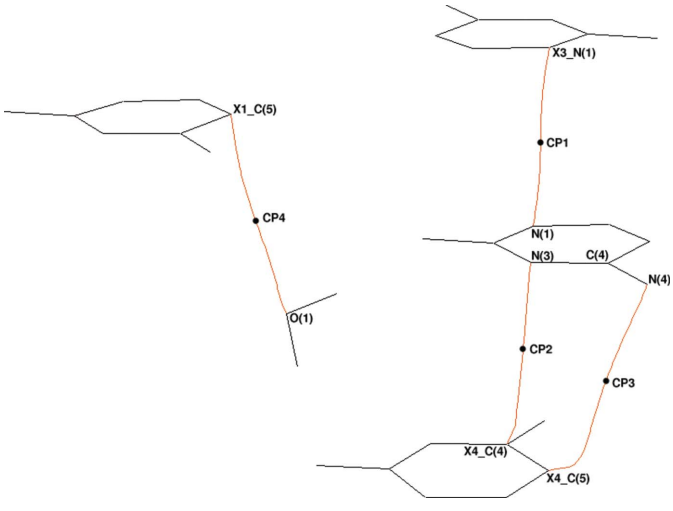

Figure 10
Bond-path character showing the BCP locations along the O···C, N···N and C···N interactions.

The networks of interactions of varying strength associated with these three molecular crystal structures generate 33 (interestingly, 11 each) intermolecular interactions in total (Tables 3, 5 and 7). On inspection of the parameters listed in

these tables, it is clear that the topological properties, such as electron density, Laplacian, local kinetic and potential energy densities, and the interpenetration of van der Waals spheres, correlate well with the length of the interaction. A similar relation is shown in our earlier studies (Munshi & Guru Row, 2005*a*,*c*; Munshi, 2005). Moreover, the agreement between experimental and theoretical results is generally good, but with some exceptions. Further, the features of these intermolecular interactions are visualized in terms of electrostatic potential (ESP) maps. Mapping of the ESP over molecular surfaces provides information on the nature and topology of the distribution of charges and allows the visualization of the deformation of molecular space in the crystalline environment. All the ESP maps plotted here are from experimental results only. In 2-thiouracil, the ESP map (Fig. 15) shows a large electronegative surface at the O atom site. However, with the present contour level (+0.30 and −0.15 e Å^{-1}) no electronegative surface was observed at the S atom site. This observation supports the well known phenomenon that the electronegativity of an S atom is much less than that of an O

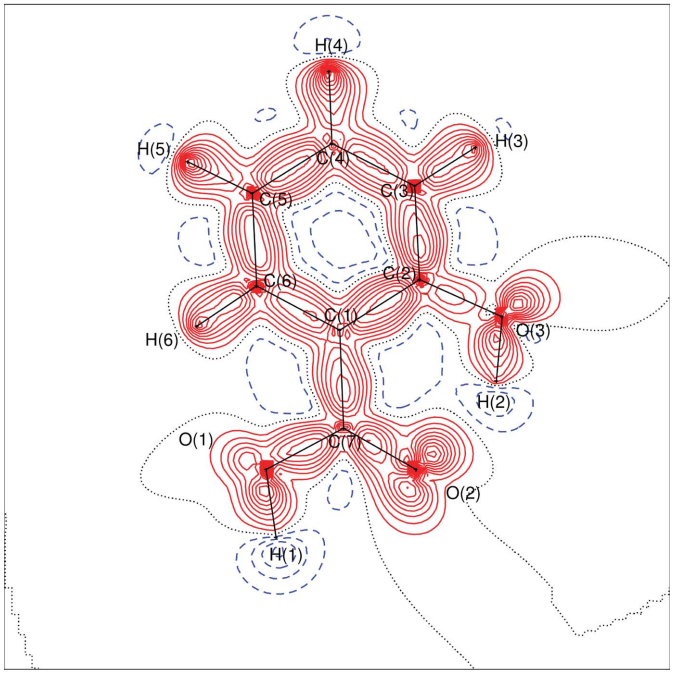

(*a*)

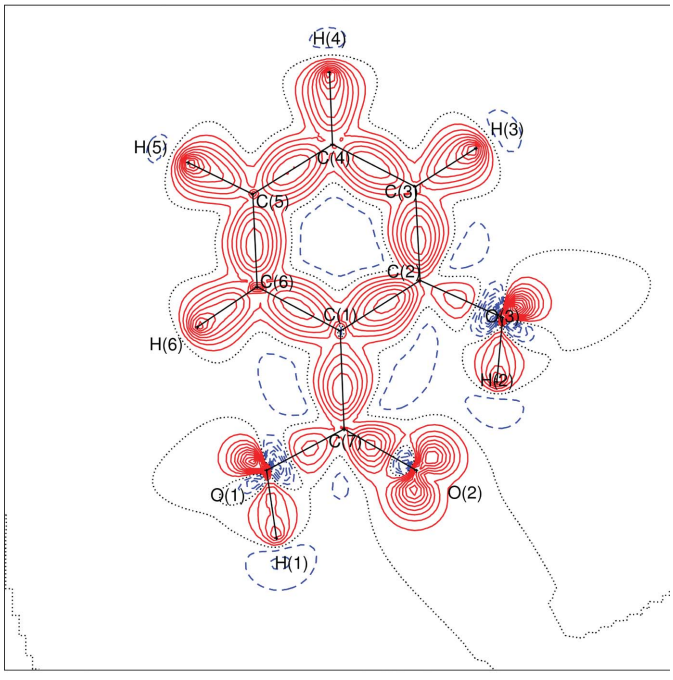

(*b*)

Figure 11
Static deformation-density maps (experimental and theoretical) for salicylic acid.

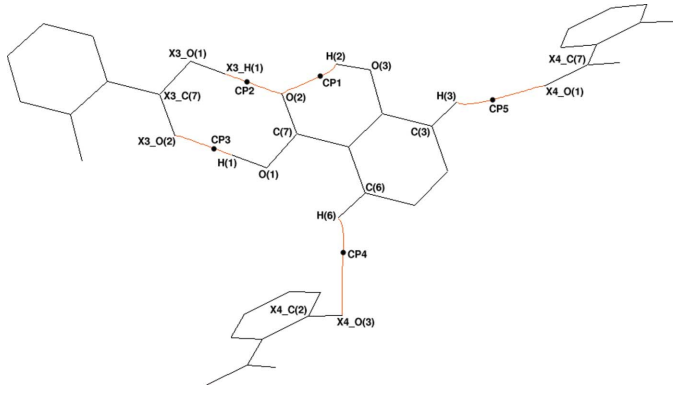

Figure 12
Bond-path character in salicylic acid showing the BCP locations along the O—H···O and C—H···O hydrogen bonds.

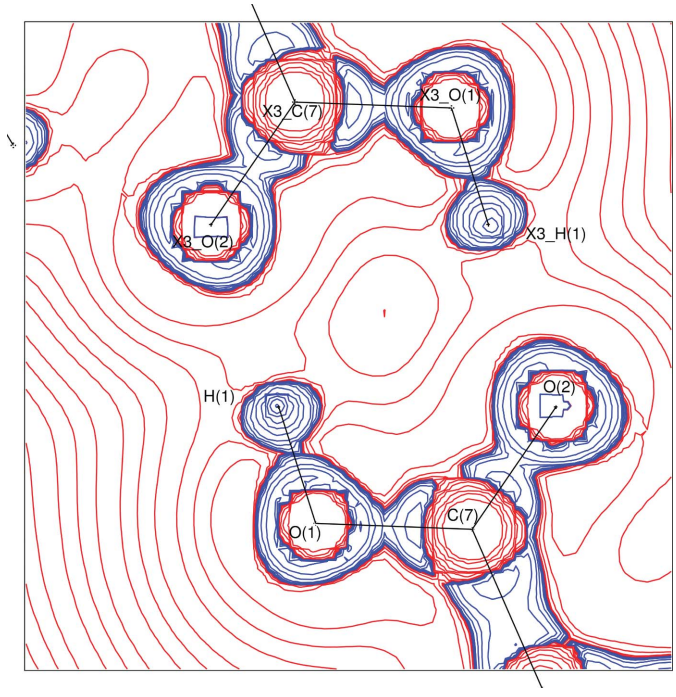

Figure 13
Laplacian [$\nabla^2\rho_b(\mathbf{r})$] distribution of the dimer formed by the O—H···O hydrogen bonds.

Table 7
The parameters characterizing the intra- and intermolecular interactions in salicylic acid (values from the periodic calculation using the B3LYP/6-31G** method are given in italics).

Interaction	$\Delta r_D - \Delta r_A$	$\Delta r_D + \Delta r_A$	R_{ij}	ρ_b	$\nabla^2\rho_b$	$G(r_{CP})$	$V(r_{CP})$
H2—O2	0.247	0.938	1.802	0.23	4.03	99.58	−89.43
x, y, z (intra)	*0.173*	*0.945*	*1.795*	*0.24*	*4.05*	*101.57*	*−92.78*
H1—*X*3···O2	0.325	1.113	1.627	0.23	5.78	132.01	−106.52
$-x+2, -y, -z$	*0.233*	*1.113*	*1.627*	*0.29*	*5.79*	*144.49*	*−131.19*
H3—*X*4···O1	0.050	0.235	2.505	0.05	0.82	16.87	−11.41
$x-1, -y+\frac{1}{2}, z+\frac{1}{2}$	*0.045*	*0.217*	*2.523*	*0.05*	*0.78*	*16.03*	*−10.79*
H6—*X*4···O3	0.042	0.087	2.653	0.04	0.67	13.83	−9.29
$x, -y+\frac{1}{2}, z-\frac{1}{2}$	*0.029*	*0.085*	*2.655*	*0.04*	*0.64*	*13.22*	*−8.9*
O2—*X*3···C7	−0.283	0.224	3.166	0.04	0.50	10.25	−6.88
$-x+1, -y, -z$	*−0.227*	*0.140*	*3.250*	*0.04*	*0.51*	*10.42*	*−7.05*
O2—*X*3···O2	−0.001	−0.289	3.369	0.03	0.50	10.18	−6.68
$-x+1, -y, -z$	*0.000*	*−0.288*	*3.368*	*0.03*	*0.54*	*10.99*	*−7.17*
O1*X*3···O3	0.000	−0.297	3.376	0.02	0.36	7.12	−4.43
$-x+1, -y, -z$	*−0.002*	*−0.296*	*3.376*	*0.02*	*0.38*	*7.43*	*−4.65*
O2—*X*1···C3	−0.318	−0.129	3.519	0.03	0.35	7.08	−4.54
$x-1, y, z$	*−0.25*	*−0.113*	*3.503*	*0.03*	*0.38*	*7.81*	*−5.19*
O3—*X*2···C4	−0.297	−0.147	3.537	0.02	0.35	6.94	−4.34
$-x+1, y-\frac{1}{2}, -z+\frac{1}{2}$	*−0.297*	*−0.147*	*3.537*	*0.02*	*0.35*	*6.94*	*−4.34*
O1—*X*1···C5	−0.155	−0.172	3.562	0.02	0.29	5.75	−3.62
$x+1, y, z$	*−0.159*	*−0.162*	*3.552*	*0.03*	*0.30*	*6.13*	*−4.07*
C1—*X*1···C3	−0.127	0.134	3.566	0.03	0.33	6.78	−4.46
$x+1, y, z$	*−0.125*	*0.098*	*3.602*	*0.03*	*0.40*	*8.40*	*−5.87*
O1—*X*1···C1	−0.181	−0.195	3.585	0.02	0.30	5.95	−3.79
$x+1, y, z$	*−0.139*	*−0.183*	*3.573*	*0.03*	*0.34*	*6.89*	*−4.51*

atom. For cytosine monohydrate, the ESP map (Fig. 16) clearly emphasizes the features of the intermolecular interactions associated with the structure. A large electronegative surface is observed at the O-atom site and it continues towards the O and N atoms of the cytosine moiety. The electropositive surfaces are all well separated. The preferred binding sites at the O atom of the water molecule as well as at the atoms of the cytosine molecule are clearly visible in this map. This pictorial representation of the electrostatic potential over the three-dimensional surface supports the earlier observations made by Weber & Craven (1990). In salicylic acid, the ESP map (Fig. 17) illustrates that the electropositive surface is separated from the electronegative surfaces. The maximum spread of the electronegative surface in the molecule is seen in the O2 atom, which participates in the strongest O—H···O hydrogen bond and in one intramolecular interaction (Table 7) with H2. These maps clearly point out the favorable binding sites available in the structures. It is expected that the mapping of ESPs from theoretical calculations and the comparison with the experimental results would provide more insight toward the interaction features and the binding sites. This work is currently under progress.

4. Conclusions

The experimental and theoretical analyses of the topological features in the three small bioactive molecules have clearly brought out the quantitative features distinguishing the strong hydrogen bonds from weak interactions. Since the H atoms are crucial in the evaluation of all these interactions, the similarities in the charge-density distributions derived from both theory and experiment point out that the quality of the X-ray data at 90 K is substantial and adequate. It is interesting to note that even in the presence of strong hydrogen bonds the nature of the weak interactions remains unaltered, indeed the weak interactions also play a major role in directing the packing of the molecules in the crystal lattice. The use of Bader's AIM theory and the criteria of KP allows for a

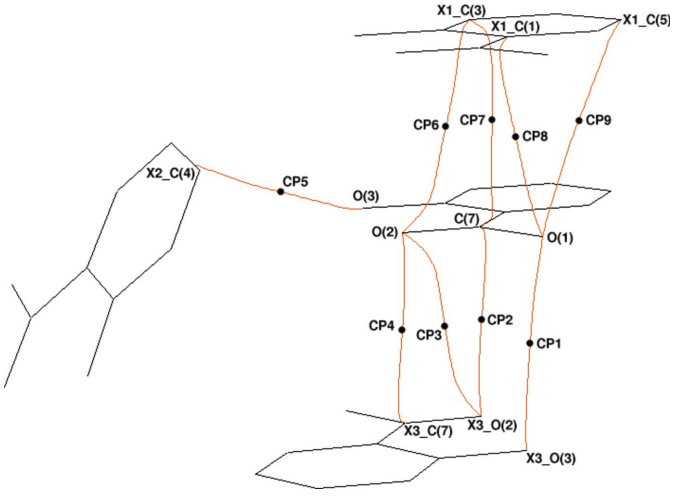

Figure 14
Bond-path character showing the BCP locations along the O···C, C···C and O···O interactions.

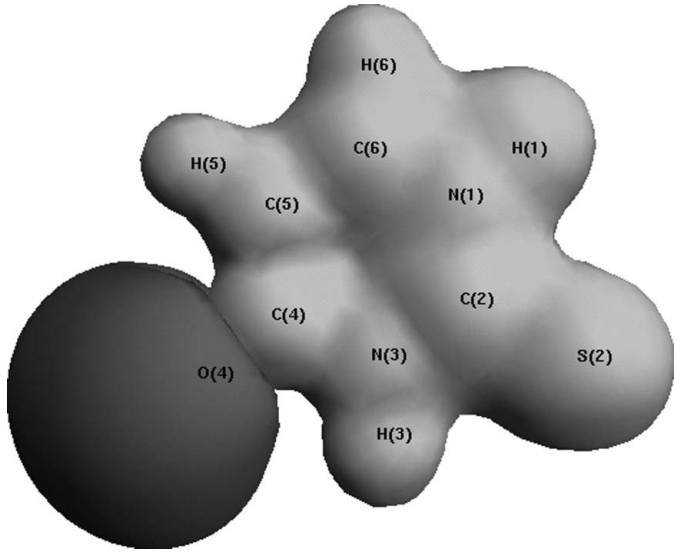

Figure 15
Molecular electrostatic potential in 2-thiouracil, the potential of +0.30 e Å^{-1} is shown as the light gray isosurface while −0.15 e Å^{-1} is shown as the dark gray isosurface.

quantitative estimate of the weak van der Waals interactions over the strong hydrogen bonds. To the best of our knowledge this is the first report on S···S interactions analyzed both from experimental and theoretical charge-density studies. For all the three structures it has been observed that the agreement between the experimental and the theoretical topological values are in general good but with some exceptions. The construction of the three-dimensional electrostatic potential over the molecular surfaces seen in these three cases suggests that this approach can be extended to quantitatively evaluate the preferred orientations at the protein binding sites and the differences in the electronegativities of the atoms in the molecule. It is expected that this methodology would yield significant indicators to the study of molecular recognition at binding sites in biomolecules.

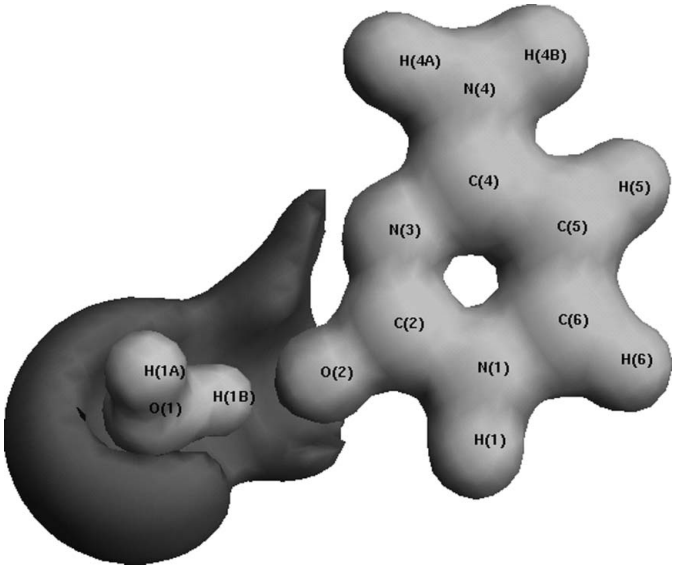

Figure 16
Molecular electrostatic potential in cytosine monohydrate, the potential of +0.40 e Å^{-1} is shown as the light gray isosurface while −0.20 e Å^{-1} is shown as the dark gray isosurface.

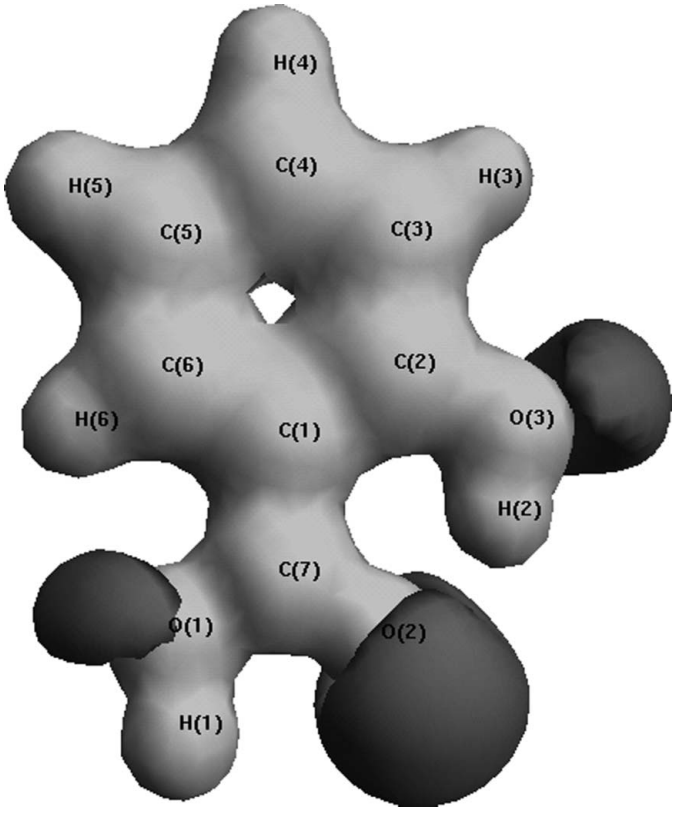

Figure 17
Molecular electrostatic potential in salicylic acid, the potential of +0.45 e Å^{-1} is shown as the light gray isosurface while −0.15 e Å^{-1} is shown as the dark gray isosurface.

P. M. thanks the CSIR, India, for senior research fellowship. We thank DST-IRHPA, India, for the CCD facility at IISc, Bangalore.

References

Allen, F. H. (1986). *Acta Cryst.* B**42**, 515–522.
Abramov, Yu. A. (1997). *Acta Cryst.* A**53**, 264–272.
Bader, R. F. W. (1990). *Atoms in Molecules – A Quantum Theory*. Oxford: Clarendon Press.
Bader, R. F. W. (1998). *J. Phys. Chem. A*, **102**, 7314–7323.
Becke, A. D. (1993). *J. Chem. Phys.* **98**, 5648–5652.
Bernstein, J., Etter, M. C. & Leiserowitz, L. (1994). *Structure Correlation*, Vol. 2, edited by H.-B. Bürgi & J. D. Dunitz, pp. 431–507. Weinheim: VCH.
Blessing, R. H. (1987). *Cryst. Rev.* **1**, 3–58.
Bondi, A. (1964). *J. Phys. Chem.* **68**, 441–451.
Braga, D., Angeloni, A., Grepioni, F. & Tagliavini, E. (1997). *Chem. Commun.* pp 1447–1448.
Bruker (2004). *SMART*, Version 5.628, and *SAINT*, Version 6.45*a*. Bruker AXS Inc., Madison, Wisconsin, USA.
Clementi, E. & Roetti, C. (1974). *At. Data Nucl. Data Tables*, **14**, 177–478.
Cochran, W. (1953). *Acta Cryst.* **6**, 260–268.
Coppens, P. (1997). *X-ray Charge Densities and Chemical Bonding*. New York: Oxford University Press.
Dahaoui, S., Pichon-Pesme, V., Howard, J. A. K. & Lecomte, C. (1999). *J. Phys. Chem. A*, **103**, 6240–6250.
Derewenda, Z. S., Lee, L. & Derewenda, U. (1995). *J. Mol. Biol.* **252**, 248–262.
Desiraju, G. R. (1991). *Acc. Chem. Res.* **24**, 290–296.
Desiraju, G. R. & Steiner, T. (1999). *The Weak Hydrogen Bond in Structural Chemistry and Biology*, pp. 253–266. Oxford University Press.
Eisenstein, M. (1988). *Acta Cryst.* B**44**, 412–426.
Espinosa, E., Alkorta, I., Elugero, J. & Molins, E. (2002). *J. Chem. Phys.* **117**, 5529–5542.
Espinosa, E. & Molins, E. (2000). *J. Chem. Phys.* **113**, 5686–5694.
Espinosa, E., Molins, E. & Lecomte, C. (1997). *Phys. Rev. E*, **56**, 1820–1833.
Espinosa, E., Molins, E. & Lecomte, C. (1998). *Chem. Phys. Lett.* **285**, 170–173.
Farrugia, L. J. (1997). *J. Appl. Cryst.* **30**, 565.
Farrugia, L. J. (1999). *J. Appl. Cryst.* **32**, 837–838.
Guru Row, T. N. (1999). *Coord. Chem. Rev.* **183**, 81–100.
Hansen, N. K. & Coppens, P. (1978). *Acta Cryst.* A**34**, 909–921.
Hariharan, P. C. & Pople, J. A. (1973). *Theor. Chim. Acta*, **28**, 213–222.
Hohenberg, P. & Kohn, W. (1964). *Phys. Rev. B*, **136**, 864–871.
Hirshfeld, F. L. (1971). *Acta Cryst.* B**27**, 769–781.
Hirshfeld, F. L. (1976). *Acta Cryst.* A**32**, 239–244.
Hirshfeld, F. L. (1977). *Isr. J. Chem.* **16**, 226–229.
Johnson, C. K. (1965). *ORTEP*. Report ORNL-3794. Oak Ridge National Laboratory, Tennessee, USA.

Jeffrey, G. A. & Saenger, W. (1991). *Hydrogen Bonding in Biological Structures.* Berlin: Springer.
Koch, U. & Popelier, P. L. A. (1995). *J. Phys. Chem.* **99**, 9747–9754.
Koritsanszky, T. S. & Coppens, P. (2001). *Chem. Rev.* **101**, 1583–1621.
Koritsanszky, T. S., Flaig, R., Zobel, D., Krane, H.-G., Morgenroth, W. & Luger, P. (1998). *Science*, **279**, 356–358.
Koritsanszky, T. S., Howard, S., Macchi, P., Gatti, C., Farrugia, L. J., Mallinson, P. R., Volkov, A., Su, Z., Richter, T. & Hansen, N. K. (2003). *XD*, Version 4.10, July. Free University of Berlin, Germany, University of Wales, Cardiff, Università di Milano, Italy, CNR-ISTM, Milano, Italy, University of Glasgow, Scotland, State University of New York, Buffalo, University of Nancy, France.
Lee, C., Yang, W. & Parr, R. G. (1998). *Phys. Rev. B*, **37**, 785–89.
Munshi, P. (2005). PhD Thesis. Indian Institute of Science, Bangalore.
Munshi, P. & Guru Row, T. N. (2002). *Acta Cryst.* B**58**, 1011–1017.
Munshi, P. & Guru Row, T. N. (2003). *Acta Cryst.* B**59**, 159.
Munshi, P. & Guru Row, T. N. (2005*a*). *J. Phys. Chem. A*, **109**, 659–672.
Munshi, P. & Guru Row, T. N. (2005*b*). *Cryst. Rev.* **11**, 199–241.
Munshi, P. & Guru Row, T. N. (2005*c*). *CrystEngComm*, **7**, 608–611.
Munshi, P. & Guru Row, T. N. (2006*a*). *Acta Cryst.* B**62**, 118–127.
Munshi, P. & Guru Row, T. N. (2006*b*). *Cryst. Growth Des.* **6**, 708–718.
Musah, R. A., Jensen, G. M., Rosenfield, R. J., McRee, D. E., Goodin, D. B. & Bunte, S. W. (1997). *J. Am. Chem. Soc.* **119**, 9083–9084.
Nyburg, S. C. & Faerman, C. H. (1985). *Acta Cryst.* B**41**, 274–279.
Oddershede, J. & Larsen, S. (2004). *J. Phys. Chem.* A**108**, 1057–1063.
Overgaard, J. & Hibbs, D. E. (2004). *Acta Cryst.* A**60**, 480–487.
Popelier, P. L. A. (2000). *Atoms in Molecules. An Introduction*, pp 150–153. New York: Prentice Hall.
Saunders, V. R., Dovesi, R., Roetti, C., Causa, M., Harrison, N. M., Orlando, R. & Zicovich-Wilson, C. M. (2003). *CRYSTAL03 1.0 User's Manual.* University of Torino, Italy.
Sheldrick, G. M. (1997). *SHELXS*97 and *SHELXL*97. University of Göttingen, Germany.
Spackman, M. A. (1992). *Chem. Rev.* **92**, 1769–1797.
Spackman, M. A. (1997). *Annu. Rep. Prog. Chem. Sect. C: Phys. Chem.* **94**, 177–207.
Steiner, T. & Saenger, W. (1992). *J. Am. Chem. Soc.* **114**, 10146–10154.
Steiner, T. & Saenger, W. (1993). *J. Am. Chem. Soc.* **115**, 4540–4547.
Stewart, R. F. (1976). *Acta Cryst.* A**32**, 565–574.
Sundaralingam, M. & Jensen, L. H. (1965). *Acta Cryst.* **18**, 1053–1058.
Tiekink, E. R. T. (1998). *Z. Kristallogr.* **187**, 79–84.
Tsernoglou, D. (1967). *Diss. Abstr. B*, **27**, 2603–2604.
Tsirelson, V. G. & Ozerov, R. P. (1996). *Electron Density and Bonding in Crystals.* Bristol: Institute of Physics Publishing.
Weber, H. P. & Craven, B. M. (1990). *Acta Cryst.* B**46**, 532–538.
Weber, H. P., Craven, B. M. & McMullan, R. K. (1980). *Acta Cryst.* B**36**, 645–649.
Yavin, M. & Folk, W. R. (1975). *J. Bol. Chem.* **250**, 3243–3253.